Comparison of vibrocompaction methods by numerical simulations

M. Arnold & I. Herle
Institute of Geotechnical Engineering, TU Dresden, Germany

J. Wehr
Keller Holding GmbH, Offenbach, Germany

ABSTRACT: Soils can be best compacted by repeated shearing. The strain amplitude plays an important role for the maximum compaction that can be reached. Experimental evidence emphasizes a vital impact of simultaneous multidirectional shear loading on the rate and magnitude of soil compaction. Two different vibrocompaction methods were analysed by numerical simulations in the light of these findings. In an elastic FE analysis strain paths were determined. A strain amplitude-dependent stiffness at small strains was introduced by multiple runs of the FE calculation to reach an appropriate stiffness for particular distances from the vibrator. Subsequently, the obtained strain paths were used to control single element simulations using hypoplasticity with intergranular strains. The calculated compaction profiles show three zones known from practical evidence: a limited compaction close to the vibrator, a zone of maximum compaction and a non-densified zone remote from the vibrator. The deep vibrator produces a faster compaction than the top vibrator, especially in the more distant zone. The more efficient work of the deep vibrator can be attributed to a more general multi-directional shearing.

1 INTRODUCTION

The mechanical behaviour of granular soils is markedly influenced by their density. Loose soils are softer and can mobilize less shear resistance than dense soils. Loose soils are usually less uniform and tend to liquefaction. Consequently, there is a demand for the densification of loose granular soils for construction purposes.

The method of vibrocompaction is being used with success for many years. The densification of soil is achieved with a vibrator oscillating during its stepwise lifting. A detailed description can be found e. g. in (Sondermann and Wehr 2004). There is a large amount of an empirical knowledge related to this method. Nevertheless, a detailed understanding of the compaction process and the role of substantial impact factors is still missing.

This paper presents results of numerical computations of the vibrocompaction method comparing horizontally circling deep vibrators and vertically oscillating top vibrators. First, a dynamical 3-D simulation of elastic medium within a disc-shaped domain produced a loading sequence for several selected points around the vibrator. Subsequently, the strain paths obtained were used for a control of numerical element tests with a hypoplastic constitutive model. A special emphasis was put on the role of the shearing mode implied by different types of deep vibrators.

2 SOIL COMPACTION BY SHEARING

It is a well established experience that granular soils can be better compacted by shearing than by all-round pressure. Youd (1972) demonstrated with a series of simple shear tests on Ottawa sand that a limiting minimum void ratio is asymptotically approached for repeated shearing. The rate of compaction depends primarily on shear strain amplitude $\Delta\gamma$. If $\Delta\gamma$ is too low (in the mentioned case if $\Delta\gamma < 0.13\%$), the minimum void ratio cannot be reached even for 10^5 cycles. On the other hand, for large strain cycles a maximum densification cannot be achieved as well due to the onset of dilatancy within each cycle (Muir Wood and Budhu 1980). Moreover, the applied shear stress should change its sign (shear reversal) in order to produce a satisfactory rate of densification (Brown 1996). Without any shear component, i.e. for purely hydrostatic stress cycles, the rate of compaction is quite small (Ko and Scott 1967).

Granulometric properties represented by grain size distribution, grain shape and grain surface are decisive for the compaction success. The rate of compaction is faster for well-graded soils than for uniformly graded ones (Wichtmann et al. 2005). A decrease of grain sphericity and/or roundness yields higher limit void ratios (Youd 1973; Gye-Chun et al. 2006).

Preceded by a thorough literature review, Wichtmann et al. (2005, 2007b) conducted a complex test-

ing programme on soil behaviour during cyclic loading at a constant radial stress. It confirmed the crucial role of strain amplitude in uniaxial shearing. Furthermore, the rate of strain accumulation increased with decreasing mean stress and increasing stress ratio, and there were additional effects like cyclic preloading influencing the results. The direction of accumulation (the ratio between the accumulated shear and volumetric strain) depended solely on stress ratio.

The problem of soil densification during pile driving, which is a similar process like vibrocompaction, was experimentally investigated by Bement and Selby (1997). They emphasized the role of stress level (reduction of compaction for increasing stress) and of granulometric properties. The importance of the stress level (mean stress) was a new aspect since it seemed to be negligible from other previous studies (Silver and Seed 1971).

The effect of shearing mode is of a fundamental significance for the performance of deep vibrocompaction. Is it sufficient to apply shear cycles in one direction only (analogously to pile vibration) or can we get a better performance by adding a second shear component in a perpendicular plane? Laboratory tests for this setup are difficult and rare.

A pioneering examination of this question undertook Pyke et al. (1975) in shaking table experiments. They compared a densification of sand in a box subjected to shaking in one, two and three, respectively, directions simultaneously. The measured settlements caused by shaking increased proportionally to the number of shaking directions, thus showing an important contribution of additional shearing planes.

Ishihara and Yamazaki (1980) performed a series of laboratory tests on sand in a simple shear device under undrained conditions. They applied shear cycles in two perpedicular directions which resulted in elliptic stress paths. The maximum rate of pore water pressure generation, which agrees qualitatively with the rate of densification, was obtained when both shear stresses were equal.

Wichtmann et al. (2007a) used a triaxial cell and a cyclic multidimensional simple shear (CMDSS) apparatus enabling load cycles with different shapes of the out-of phase strain loops. They confirmed that out-of-phase cycles (i.e. elliptic stress paths in the p'-q-stress plane) produce higher accumulation rates than in-phase cycles (i.e. linear stress paths in p'-q-stress plane) with a same strain amplitude. Also a sudden change of the polarisation yields a faster strain accumulation rate.

Consequently, the described experimental evidence emphasizes a vital impact of simultaneous multidirectional shear loading on the rate and magnitude of soil compaction.

3 NUMERICAL MODELLING

The compaction of soil is equivalent with a reduction of the volume of voids, the latter being usually described by void ratio. Hence, constitutive models applied for the simulation of compaction processes should, besides other requirements, incorporate void ratio or an analogous parameter.

Hypoplastic models include void ratio as a state variable and, thus, they well meet the above mentioned condition. In order to simulate cyclic stress and strain paths in coarse grained soils, a version of the hypoplastic model by von Wolffersdorff (1996) with the intergranular strain enhancements of Niemunis and Herle (1997) can be used.

3.1 *Simulations of Keßler et al.*

Keßler et al. (2006) simulated strain paths in soil due to vibrocompaction with a deep vibrator in a linear elastic medium. At first, they studied the impact of different FE model geometries (Fig. 1) on the calculated strains. They compared (a) a full 3D model with a rotating vibrator, (b) a 3D disc-shaped soil section under a constant vertical stress with a rotating vibrator and (c) an axisymmetric model with displacement-controlled expansion of a cylinder.

The strain paths calculated using the 3D models (a) and (b) were relatively similar, while the strain paths generated by the axisymmetric model (c) were quite different compared to the both previous ones. Provided that the full 3D model (a) yields strain paths closest to reality, the disc-shaped-model (b) can be used as a reasonable simplification. It can be considered as a compromise between the model quality and the computational effort. The axisymmetric model (c) seems to be not appropriate for modelling vibrocompaction with deep vibrators.

3.2 *Calculation procedure*

A dynamic FE calculation using a 3D geometry together with a hypoplastic model with intergranular strains would be a suitable method to simulate vibrocompaction. However, there are at least two drawbacks with this approach: Firstly, there is little experience using this constitutive model in dynamic calculations, yet. Secondly, the computational effort is enormous — even a 3D disc-shaped model like in Fig. 1b) requires a very long computational time.

Therefore, a calculation procedure analogous to (Keßler et al. 2006) was chosen. In the first step, a dynamic finite element analysis was performed in order to obtain strain paths. The FE code Tochnog (2006) was used for the elastic analysis of a 3D disc-shaped model. The solution was carried out in the time domain. In the second step, the strain paths obtained were used as an input for hypoplastic element calculations simulating the densification process.

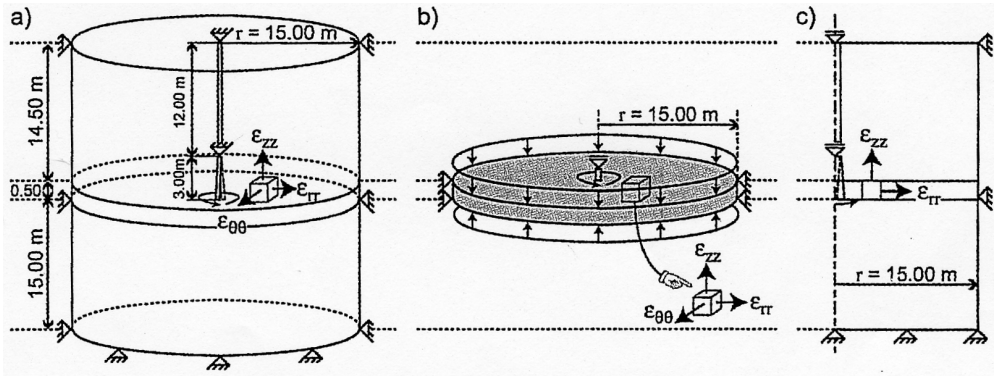

Figure 1: FE models: (a) a full 3D model with rotating vibrator, (b) 3D disc-shaped soil section (c) axisymmetric model (Keßler et al. 2006).

3.3 *Constitutive Modelling*

The soil was modelled by the hypoplasticity with intergranular strains (Niemunis and Herle 1997; von Wolffersdorff 1996) using the parameter set of Keßler et al. (2006) (Table 1). This enabled a comparison with the published results (Keßler et al. 2006).

Table 1: Hypoplastic constitutive constants.

φ_c	h_s in MPa	n	e_{d0}	e_{c0}	e_{i0}	α
32.5°	591	0.50	0.577	0.874	1.005	0.12
β		R	m_R	m_T	β_r	χ
1.0		$1{\cdot}10^{-4}$	2.9	1.45	0.2	6.0

The initial density of the soil was assumed to be very low. An initial void ratio e_0 of 0.85 was chosen. A dry density of 1.43 g/cm^3 was obtained with an assumed particle density of 2.65 g/cm^3 (quartz sand).

Like shown by Niemunis and Herle (1997), the constitutive model is able to reproduce a realistic degradation of shear stiffness with strain. Using the chosen constitutive constants, numerical biaxial tests were conducted to simulate the stiffness degradation for different states of the strain history. The initial void ratio was set to 0.85 and the isotropic initial stress state to $\sigma_{11} = \sigma_{22} = \sigma_{33} = -0.14$ MPa. This corresponds to an average stress at the modelled depth of 15 m. Different strain histories were introduced by an appropriate initialization of the state variable intergranular strain. Fig. 2 shows the secant modulus $G_{sec} = (\sigma_{11} - \sigma_{22})/(\varepsilon_{11} - \varepsilon_{22})$ plotted versus shear strain $\Delta\gamma = |\varepsilon_{11} - \varepsilon_{22}|$.

Hardin and Drnevich (1972) presented a widespread equation of the stiffness degradation with strain. Recently, a modified approach was suggested by Hardin and Kalinski (2005):

$$G_{sec}(\Delta\gamma) = \frac{G_{sec,0}}{1 + \frac{\Delta\gamma}{\gamma_r}\left(1 + a \cdot \exp\left[-b\frac{\Delta\gamma}{\gamma_r}\right]\right)} \qquad (1)$$

Eq. 1 was used to fit the curve of a strain reversal (180° curve) of Fig. 2 via the parameters $G_{sec,0}$, γ_r and a. The parameter b was set to 1 like proposed by Hardin and Kalinski (2005). The best fit yielded parameter $a < -1$ resulting in an initial increase of the shear modulus with strain. Because of this contradiction to the observed behaviour, a was set to -1 to ensure a monotonic decrease of the shear stiffness with strain. $G_{sec,0} = 110$ MPa and $\gamma_r = 2.2 \cdot 10^{-3}$ were obtained from this fit.

The fit of Eq. 1 was used to create a link between the hypoplasticity and elasticity with variable stiffness. Provided that there is a cyclic shear strain loading $\gamma(t) = \gamma_A \cdot \cos(\omega t)$ (Fig. 3a), the shear strain direction reverses at $t = 0$. $\Delta\gamma$ in Eq. 1 increases from zero at $t = 0$ to $2 \cdot \gamma_A$ at $t = \pi/\omega$. Hence, the shear stiffness starts at $G_{sec,0}$ and decreases with strain to a value of $G_{sec}(2 \cdot \gamma_A)$ at $t = \pi/\omega$ (Fig. 3b). At this time, the direction reverses again. $\Delta\gamma$ starts from zero and

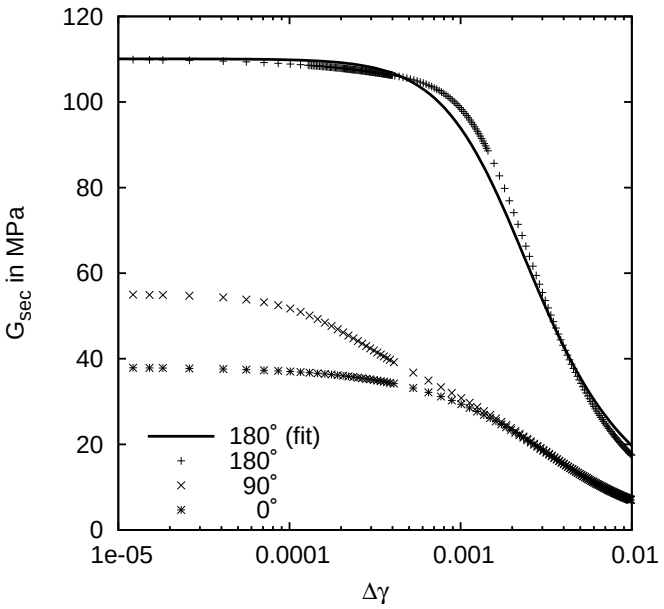

Figure 2: Calculated secant stiffness for a biaxial compression with constant volume after a change of strain path direction.

the shear stiffness degradation starts once again from $G_{sec,0}$.

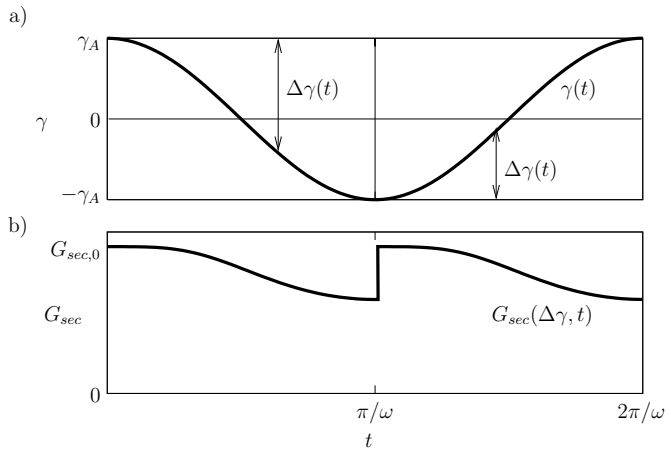

Figure 3: a) Shear strain vs. time, b) secant shear modulus vs. time during one strain cycle.

Based on the relationship between G_{sec} and $\Delta\gamma$, it is possible to assign to each material point, which is oscillating with a shear strain amplitude γ_A, a corresponding shear modulus G_{sec}. Since the shear strain amplitude is not known a priori, it has to be iteratively approached by multiple runs of the elastic FE calculation. The shear modulus G^i_{sec} of the run i follows from γ_A^{i-1} of the previous run $(i-1)$. The Poisson's ratio of 0.28 was kept constant.

4 FE MODEL OF DYNAMIC ANALYSIS

4.1 *Geometry and discretization*

A 3D disc-shaped model similar to that in Fig. 1 (b) was used. It has an exterior radius of 15 m and a height of 0.5 m. It represents a soil layer which is located at a depth between 14.5 and 15 m below the ground surface. The soil volume is discretized by 4-node tetrahedral elements. The irregular mesh consisting of more than 12,000 elements is shown in Fig. 4. The maximum length of an element side is 0.7 m. This is approx. $1/3$ of the ocurring smallest wave length and therefore sufficient to capture the propagation of the waves. The vibrator has a radius of 0.2 m and a length of 3.0 m. It was not discretized. Instead, a cylindric hole in the disc at the position of the vibrator was considered (see zoom in Fig. 4).

Due to the geometry of the model it is convenient to use a cylindrical coordinate system. The disc spreads in the plane described by the polar coordinates r and ϑ. The symmetry axis of the disc coincides with the axis z.

4.2 *Boundary conditions*

All nodes at the circumference were fixed in the horizontal direction. The nodes at the bottom of the circumference were additionally fixed vertically. For the sake of stress equivalence to the real 3D situation, the disc was perpendicularly loaded at the top and at the bottom with an average vertical stress in this depth, even though this does not influence the calculated strains in the elastic model.

The movement of the vibrator was simulated by velocity boundary conditions at the surface nodes of the cylindric hole. The deep vibrator was assumed to be hinged at its top (2.5 m above the disc surface). Thus, the surface nodes were moved along a circular path with a radius of 7.5 mm at the bottom and of 6.25 mm at the top of the disc. The applied frequency was 30 Hz.

To model a vertically oscillating top vibrator, the surface nodes of the cylindric hole were moved vertically with an amplitude of 7.5 mm. No attention was paid to the contact between the soil and the vibrator. Hence, no information on the mobilization of friction between the vibrator and the soil was obtained. Consequently, a more efficient compaction than in reality can be expected in the calculations, since unproductive slip effects at the interface are excluded in this simplified model.

4.3 *Stiffness iteration*

Several calculation steps were needed in order to get a consistent distribution of the strain-dependent stiffness within the discretized domain. Each step consisted of an initial static cycle and subsequent 90 dynamic cycles. In the initial step, a constant Young's modulus following from the initial shear modulus $G_{sec,0}$ was assumed (see section 3.3).

The strain paths with all six components of the strain tensor were registered in eight points along the radial direction of the model. After 60 cycles the transient effects vanished and the oscillation amplitudes of all six strain components became steady and could be generalized. A scalar shear strain amplitude γ_A was obtained from the maximum second invariant of the strain tensor. The resulting stiffness could be calculated at the selected eight points using Eq. 1.

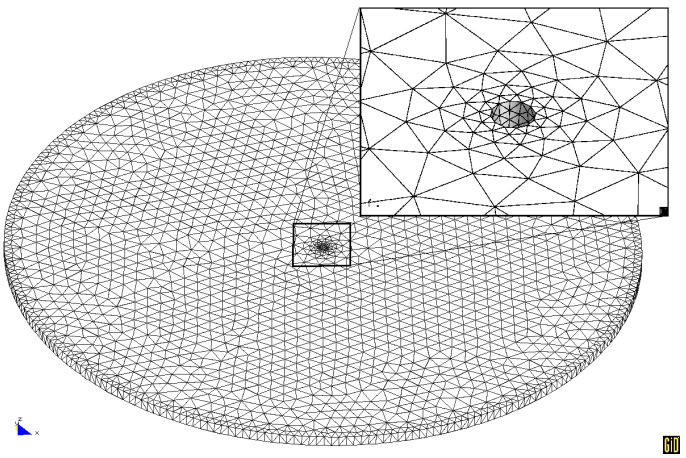

Figure 4: FE mesh.

In the next step, a strain-dependent stiffness was distributed along the radial direction using a multi-linear function. Nine additional steps were performed in this way. A fast convergence was observed within the iteration process.

5 RESULTS OF DYNAMIC ANALYSIS

At time $t = 1$ s the initial equilibrium iteration is finished and the calculation starts with a static cycle until $t = 1.033$ s. 90 dynamic cycles with a total duration of three seconds follow. The response of a point at a radius of 4.4 m located in a depth of 14.75 m was chosen as an example.

5.1 *Time-dependence of velocities*

Fig. 5 shows three components of the velocity vector. At the beginning of the calculation, a transient effect can well be recognised in the radial velocity v_r as well as in the circumferential velocity v_ϑ. This transient effect results from the activation of inertia after the static initial cycle. After approximately 60 cycles ($t > 3$ s), the oscillations reach more or less a steady state with a 30 Hz frequency corresponding to the one of the excitation.

5.2 *Time-dependence of strains*

Figures 6 (a) and (b) show the evolution of strains. A similar transient effect is observed as for the velocities. At later cycles one can notice secondary frequencies apart from the excitation frequency, although the latter is clearly dominant. Normal strain ε_{rr} and shear strain $\varepsilon_{r\vartheta}$ exhibit the largest magnitudes, the shear strain components $\varepsilon_{\vartheta z}$ and ε_{rz} are very small.

In Fig. 6 (c) two cycles are zoomed out of Fig. 6 (b). The figure manifests the dominating excitation frequency with its sinus shape as well as the phase

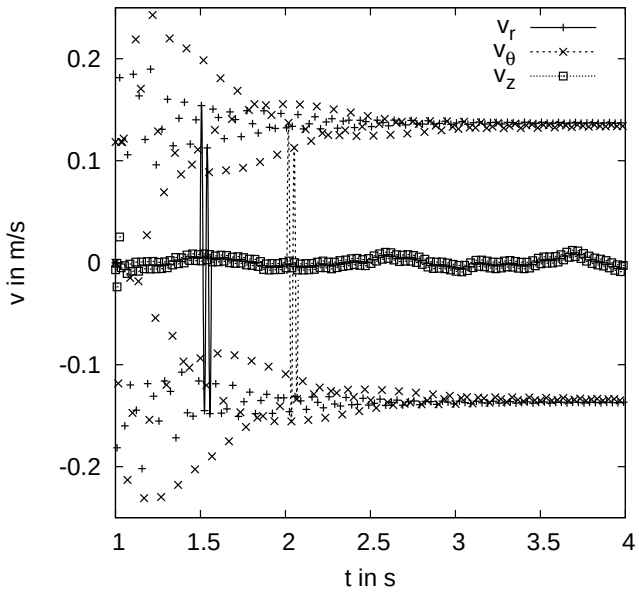

Figure 5: Envelope of maximum velocities at a distance 4.4 m from the symmetry line in the deep vibrator problem.

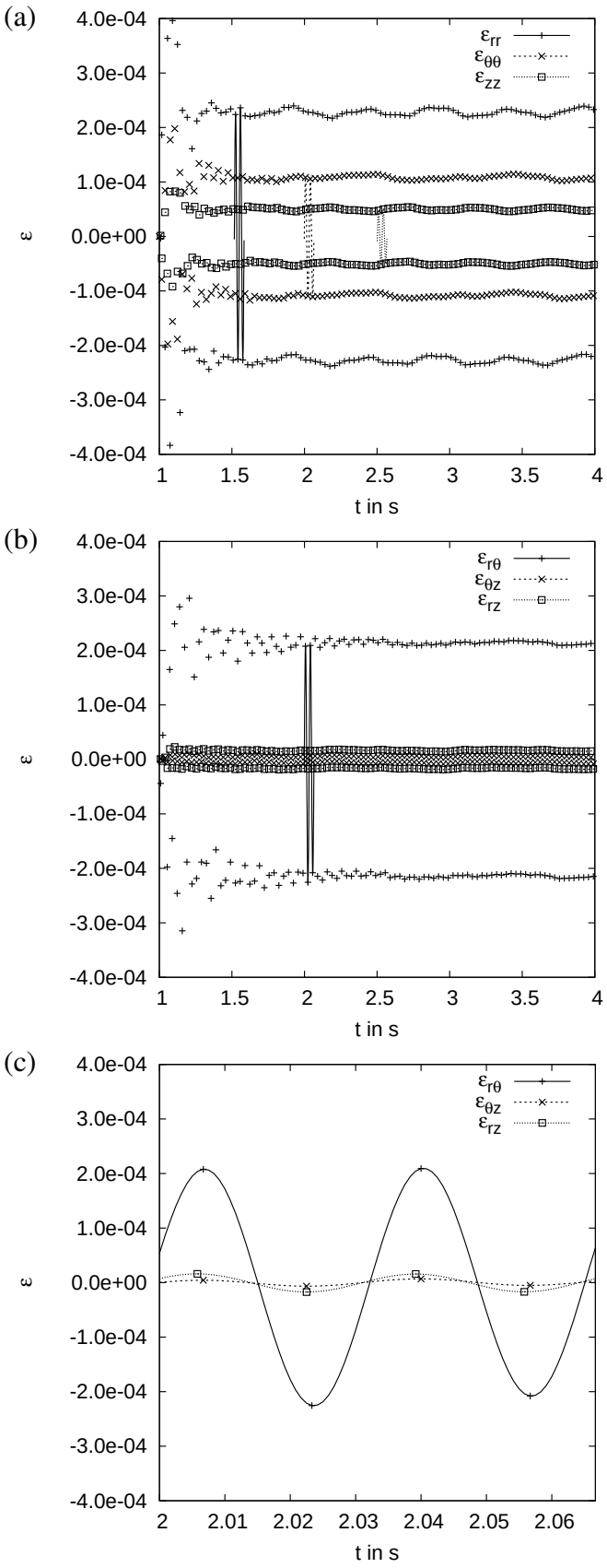

Figure 6: (a) Envelope of maximum normal strains, (b) envelope of maximum shear strains and (c) shear strains of two selected cycles at a distance 4.4 m from the symmetry line in the deep vibrator problem.

shifts, which occur due to differing wave velocities for different wave types.

Although the results presented above were obtained for the simulation of deep vibrator, the same observations and conclusions apply also for top vibrator.

5.3 *Strain path generalization*

It has been shown that the excitation frequency dominates the strains. Thus, it is meaningful to consider only this frequency. To approximate the strain path during one cycle j, the equation

$$\varepsilon_{\alpha\beta,j}(t) = a_{\alpha\beta,j} \sin\left(2\pi \frac{t}{T} + b_{\alpha\beta,j}\right) + c_{\alpha\beta,j}\, t + d_{\alpha\beta,j} \tag{2}$$

was assumed for each strain component $\varepsilon_{\alpha\beta}$ with $\alpha, \beta \in \{r, \vartheta, z\}$. The period T of a cycle was $1/30$ s. For each strain component and each cycle i from 61 to 90 (2 s $< t \leq$ 3 s) Eq. 2 was fitted to the calculated data via $a_{\alpha\beta,j}, b_{\alpha\beta,j}, c_{\alpha\beta,j}$ and $d_{\alpha\beta,j}$.

To eliminate other frequencies and a possible drift, $c_{\alpha\beta,j}$ and $d_{\alpha\beta,j}$ were disregarded. The strain amplitudes $a_{\alpha\beta,j}$ and the phase shifts $b_{\alpha\beta,j}$ were averaged over the cycles to $a_{\alpha\beta}$ and $b_{\alpha\beta}$, respectively. Hence, the approximate time dependence of the strain components after the filtering reads

$$\varepsilon_{\alpha\beta}(t) = a_{\alpha\beta} \sin\left(2\pi \frac{t}{T} + b_{\alpha\beta}\right) \tag{3}$$

5.4 *Location-dependence of strains*

The strain amplitudes obtained from the approximation (Eq. 3) are plotted for different radii in Fig. 7. Since the amplitudes differ by the order of magnitude, a logarithmic scale is used. For both vibrator types, the largest amplitudes of most strain components occur near the vibrator. With increasing distance from the vibrator the amplitudes decrease. This general pattern results predominantly from the geometrical damping. This effect is further emphasized by the strain-dependent stiffness, which is low close to the vibrator and becomes high in the outer domains of the considered disc volume.

For the same excitation amplitude, the deep vibrator tends to produce larger strain amplitudes in the soil than the top vibrator. Furthermore, the shear strains $\varepsilon_{r\vartheta}$ and $\varepsilon_{\vartheta z}$ are zero in the latter case since the top vibrator problem is — even though this was not imposed by the FE analysis — a completely radially symmetric problem. Recalling the experimental evidence from Section 2, the deep vibrator is able to achieve a better and faster densification than the top vibrator due to the application of multiaxial shearing in the first case.

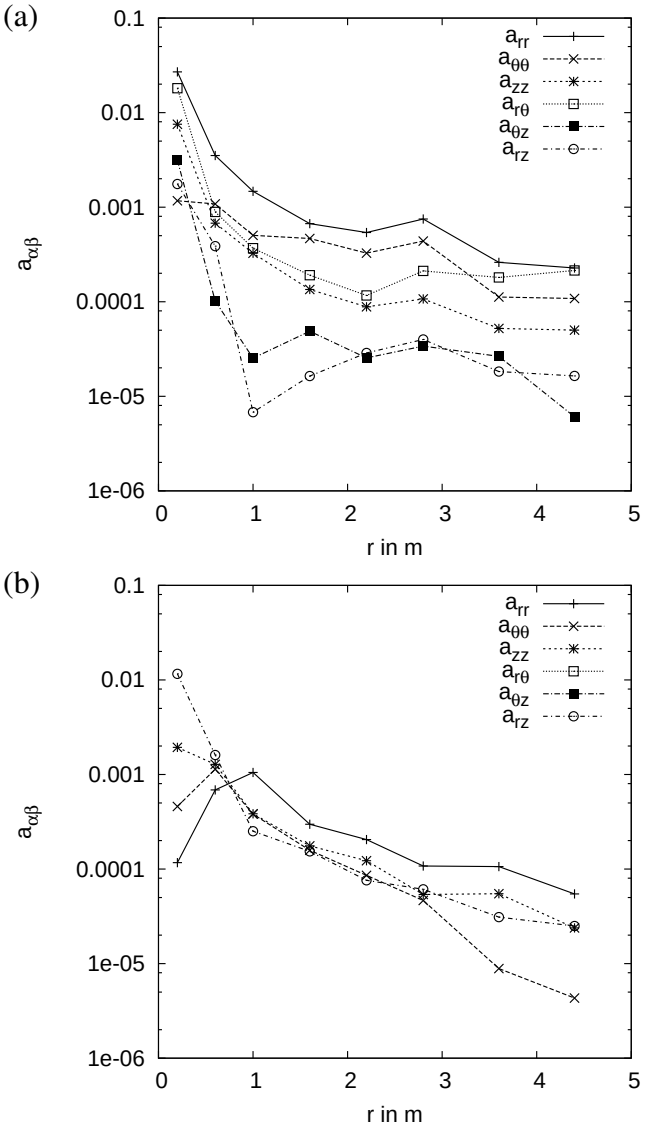

Figure 7: Magnitude of strain amplitudes (logarithmic) in the case of (a) deep vibrator and (b) top vibrator. Elastic analysis.

5.5 *Remark*

The elastic FE analyses considered a strain-dependent stiffness. This stiffness was obtained from a numerical biaxial test on loose soil. During the compaction process the soil gets denser and, hence, the stiffness increases. This stiffness increase was not taken into account by the applied model. Nevertheless, the ratio between the stiffness of a dense and a loose sand is low, usually about two (Herle and Gudehus 1999), which does not have a substantial impact on the obtained results. The considered change of the stiffness due to strain-dependence is much more pronounced, cf. Fig. 2.

6 HYPOPLASTIC ELEMENT SIMULATIONS

6.1 *Procedure*

It is assumed that a soil particle in the compacted continuum oscillates in the horizontal directions r and ϑ around a fixed position. Hence, all strains regard-

ing the horizontal position of the particle form closed loops. In the vertical direction the soil particle oscillates, too, but it also moves downward due to the densification of the grain skeleton. Consequently, the vertical strain ε_{zz} does not follow a closed loop. However, the geostatic vertical stress σ_{zz} is known and can be applied as a boundary condition in the vertical direction.

This idealization was used in the hypoplastic simulations with the element test program HYPTEST (Herle 1997). The strain paths obtained in the elastic FE analyses were applied as a test control. Since the hypoplastic model is formulated in rates, the strain rates $\dot{\varepsilon}_{rr}, \dot{\varepsilon}_{\vartheta\vartheta}, \dot{\varepsilon}_{r\vartheta}, \dot{\varepsilon}_{\vartheta z}$ and $\dot{\varepsilon}_{rz}$ were prescribed using the relationship

$$\dot{\varepsilon}_{\alpha\beta}(t) = -a_{\alpha\beta}\frac{2\pi}{T}\cos\left(2\pi\frac{t}{T} + b_{\alpha\beta}\right) \tag{4}$$

which is the time derivative of Eq. 3.

The initial void ratio of the loose soil was set to 0.85. The initial stress state was considered as $\sigma_{rr} = \sigma_{\vartheta\vartheta} = 0.1$ MPa and $\sigma_{zz} = 0.2$ MPa. For each of the eight selected points, 100 cycles have been calculated.

6.2 *Results*

The evolution of void ratio with strain cycles can be seen in Fig. 8. Starting from the initial value of 0.85, void ratio reduces with progressing cycles. The rate of the reduction decreases with time. Thus, the first 20 cycles lead to a larger change in void ratio than the second 20 cycles, and so on.

For both types of the vibrator, three zones may be distinguished. In the first zone close to the vibrator ($r < 0.5$ m), the densification fades out after only a few cycles without reaching the minimum void ratio. This effect, which has been observed also in the field application of vibrocompaction, is caused by large strain amplitudes in this domain. At the beginning of a shear deformation process, soil behaves contractant. But if shear strains grow further on, the soil becomes dilatant. Hence, contractancy and dilatancy balance each other and an overall volumetric deformation vanishes.

In the second zone within approximately 0.5 m $< r < 3.0$ m the compaction process succeeds to approach a pressure dependent minimum void ratio. Contractancy prevails and the soil reaches a densification limit. In this zone vibrocompaction works at best. The larger the distance from the vibrator, the slower the compaction progress.

For the deep vibrator as well as for the top vibrator only 60 cycles suffice to reach the densest state, while in the field application several thousand cycles are required. The model seems to predict a too fast compaction rate, probably due to the simplifying assumptions in the model formulation. E. g., the influence of pore water was disregarded. Since compaction is based on the reduction of pore volume, water has to flow out of the densified soil. Due to a final permeability even of coarse grained soils this would take certainly more time than two seconds. Probable liquefaction phenomena make the situation even more complex.

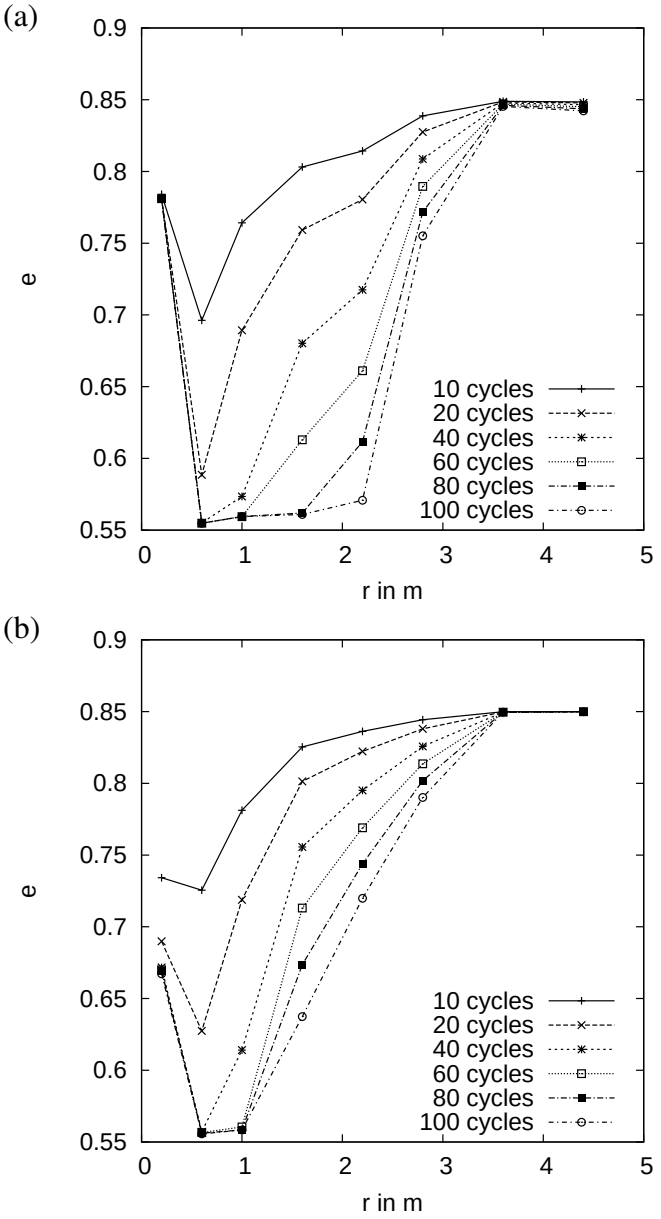

Figure 8: Evolution of void ratio along radial distance from the vibrator in the case of (a) deep vibrator and (b) top vibrator.

The third zone is characterized by a constant void ratio and spreads behind the second zone. There, strain amplitudes are too small to surpass the reversible elastic strain range. This zone is not affected by the vibrocompaction.

If one compares deep vibrator and top vibrator, the deep vibrator produces a faster compaction than the top vibrator, especially in the more distant second zone. This may be documented by the fact, that the zone compacted to a minimum void ratio after

80 cycles has a radius of 1.6 m in case of the deep vibrator, but only 1.0 m in case oftop vibrator. The more efficient work of the deep vibrator results from a more general multi-directional shearing, as already discussed before. Larger strain amplitudes of the deep vibrator boost this effect as well.

7 CONCLUSIONS

The presented results of the advanced numerical analysis of vibrocompaction comparing deep and top vibrators point out to a better performance of deep vibrators. It is achieved by a multidirectional shearing mode imposed by a combined vertical and rotational movement of the deep vibrator. The outcomes of the laboratory experiments with this type of loading support this finding.

In spite of the demanding computations within the presented analysis, several important effects were not considered: (1) The influence of pore water and thus a potential liquefaction of soil due to the undrained response during the short time of vibration. (2) A realistic interface between the vibrator and soil which can take into account slip effects after reaching the maximum shear stress at the contact. (3) A general 3-D model which does not require an assumption of constant stresses at the boundaries of the disc-shaped domain.

Due to the omitted effects mentioned above, there are discrepancies between the obtained results and experience in situ, especially regarding the evolution of densification in time. Further research should clarify the particular role of the above stated items.

ACKNOWLEDGEMENT

This work was supported by Keller Holding GmbH, which is gratefully acknowledged.

REFERENCES

Bement, R. and A. Selby (1997). Compaction of granular soils by uniform vibration equivalent to vibrodriving of piles. *Geotechnical and Geological Engineering 15*, 121–143.

Brown, S. F. (1996). Soil mechanics in pavement engineering. *Géotechnique 46*(3), 383–426.

Gye-Chun, C., J. Dodds, and J. C. Santamarina (2006). Particle shape effects on packing density, stiffness and strength: natural and crushed sands. *Journal of Geotechnical and Geoenvironmental Engineering ASCE 132*(5), 591–602.

Hardin, B. O. and V. P. Drnevich (1972). Shear modulus and damping of soils: Design equations and curves. *ASCE Journal of the Soil Mechanics and Foundations Division 98*(7), 667–692.

Hardin, B. O. and M. E. Kalinski (2005). Estimating the shear modulus of gravelly soils. *ASCE Journal of Geotechnical and Geoenvironmental Engineering 131*(7), 867–875.

Herle, I. (1997). Hypoplastizität und Granulometrie einfacher Korngerüste. Dissertation. Heft 142, Veröffentlichungen des Institutes für Bodenmechanik und Felsmechanik der Universität Fridericiana in Karlsruhe.

Herle, I. and G. Gudehus (1999). Determination of parameters of a hypoplastic constitutive model from properties of grain assemblies. *Mechanics of Cohesive-Frictional Materials 4*(5), 461–486.

Ishihara, K. and F. Yamazaki (1980). Cyclic simple shear tests on saturated sand in multi-directional loading. *Soils and Foundations 20*(1), 45–59.

Keßler, S., G. Heibrock, and T. Triantafyllidis (2006). On prediction of vibrocompaction performance using numerical models. In Gonin, Holeymann, and Rocher-Lacoste (Eds.), *Symposium International TRANSVIB 2006*, Paris, pp. 233–242. Editions du LCPC.

Ko, H.-Y. and R. Scott (1967). Deformation of sand in hydrostatic compression. *Journal of the Soil Mechanics and Foundations Division ASCE 93*(SM3), 137–156.

Muir Wood, D. and M. Budhu (1980). The behaviour of Leighton Buzzard Sand in cyclic simple shear tests. In *Int. Symposium on Soils under Cyclic and Transient Loading*, pp. 9–21. A.A.Balkema.

Niemunis, A. and I. Herle (1997). Hypoplastic model for cohesionless soils with elastic strain range. *Mechanics of Cohesive-Frictional Materials 2*(4), 279–299.

Pyke, R., H. B. Seed, and C. K. Chan (1975). Settlement of sands under multidirectional shaking. *Journal of Geotechnical Engineering Division ASCE 101*(GT4), 379–398.

Silver, M. L. and H. B. Seed (1971). Volume changes in sands during cyclic loading. *Journal of the Soil Mechanics and Foundations Division ASCE 97*(SM9), 1171–1182.

Sondermann, W. and W. Wehr (2004). Deep vibro techniques. In M. Moseley and K. Kirsch (Eds.), *Ground Improvement, 2nd edition*, pp. 57–92. Spon Press.

Tochnog (2006). Tochnog Professional Version 4.1. URL: http://www.feat.nl.

von Wolffersdorff, P.-A. (1996). A hypoplastic relation for granular materials with a predefined limit state surface. *Mechanics of Cohesive-Frictional Materials 1*(4), 251–271.

Wichtmann, T., A. Niemunis, and T. Triantafyllidis (2005). Strain accumulation in sand due to cyclic loading: drained triaxial tests. *Soil Dynamics and Earthquake Engineering 25*(12), 967–979.

Wichtmann, T., A. Niemunis, and T. Triantafyllidis (2007a). On the influence of the polarization and the shape of the strain loop on strain accumulation in sand under high-cyclic loading. *Soil Dynamics and Earthquake Engineering 27*, 14–28.

Wichtmann, T., A. Niemunis, and T. Triantafyllidis (2007b). Strain accumulation in sand due to cyclic loading: Drained cyclic tests with triaxial extension. *Soil Dynamics and Earthquake Engineering 27*, 42–48.

Youd, T. (1972). Compaction of sands by repeated shear straining. *Journal of the Soil Mechanics and Foundations Division ASCE 98*(7), 709–725.

Youd, T. (1973). Factors controlling maximum and minimum densities of sands. In *Evaluation of relative density and its role in geotechnical projects involving cohesionless soils*, STP 523, pp. 98–112. ASTM.